Langmuir

Article

pubs.acs.org/Langmuir

Assessing the Local Nanomechanical Properties of Self-Assembled Block Copolymer Thin Films by Peak Force Tapping

Matteo Lorenzoni,*[,†] Laura Evangelio,[†] Sophie Verhaeghe,[†] Célia Nicolet,[‡] Christophe Navarro,[‡] and Francesc Pérez-Murano[†]

[†]1 Instituto de Microelectrónica de Barcelona (IMB-CNM, CSIC), Campus de la UAB, 08193 - Bellaterra, Barcelona, Spain

[‡]Arkema France, R.N. 117, BP34-64170 Lacq, France

Supporting Information

ABSTRACT: The mechanical properties of several types of block copolymer (BCP) thin films have been investigated using PeakForce quantitative nanomechanical mapping. The samples consisted of polystyrene/poly(methylmethacrylate) (PS/PMMA)-based BCP thin films with different pitches both randomly oriented and self-assembled. The measured films have a critical thickness below 50 nm and present features to be resolved of less than 22 nm. Beyond measuring and discriminate surface elastic modulus and adhesion forces of the different phases, we tuned the peak force parameters in order to reliably image those samples, avoiding plastic deformation. The method is able to detect the changes in mechanical response associated with the orientation of the PMMA cylinders with respect to the substrate (parallel versus vertical). The nanomechanical investigation is also capable of recognizing local stiffening due to the preferential growth of alumina deposited by atomic layer deposition on BCP samples, opening up new possibilities in the field of hard mask materials characterization.

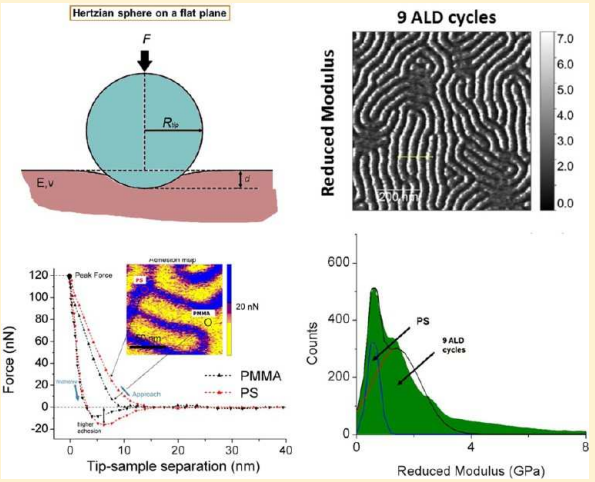

1. INTRODUCTION

Among alternative lithographic methods for the creation of ordered patterns, direct self-assembly (DSA) of block copolymer (BCP) is attracting major interest and effort.[1,2] Due to the potentially high throughput and relatively simple processing, DSA is likely to be adopted by the microelectronics industry within a few years. BCPs are macromolecules that are formed by two (or more) polymer chains (blocks) joined by interblock covalent bonds. The two phases, which are thermodynamically incompatible, have a natural tendency to separate at length scales close to the polymer's chain dimensions. Phase separation will generate nanostructured morphologies with different structural configurations (plates, cylinders, spheres, or other more complex shapes) depending on several parameters (i.e., the ratio of molecular weights of the blocks forming the copolymer).[3] The spontaneous formation of nanostructures has to be guided to obtain long-range order and the desired orientation,[4] often employing a so-called guiding pattern generated either by conventional lithography[1] or alternative methods.[5] The future employment of such structures in the semiconductor industry is thus raising new issues related to metrology and inspection.

Atomic force microscopy (AFM) can overcome the problems usually connected with nanoindentation (in which typical indentation depths range from about 10 nm to 10 μm)[6,7] by probing the very top surface (less than 10 nm), and it is broadly used to simultaneously capture surface topography on the nanometric scale and map the qualitative differences in local surface properties such as friction, adhesion, and elastic modulus on several kinds of samples, such as polymers,[8,9] paper coatings,[10] and proteins.[11] Using PeakForce quantitative nanomechanical mapping (QNM), it is possible to reliably quantify Young's modulus (E) of materials with high spatial resolution and surface sensitivity.[12] This technique is capable of acquiring a large number of force−distance curves and elaborates the curves in real time to calculate the mechanical properties at each point. We apply this technique to characterize the mechanical properties of polymer ultrathin films (thicknesses <50 nm) that are challenging to characterize and are of key interest in the area of advanced lithography and directed self-assembly of block copolymers. It is also important to mention that alongside the force−volume-based techniques, different approaches based on AFM dynamic modes[13−15] have yielded remarkable results in terms of resolution and acquisition speed.[16]

When probing ultrathin films, film thickness is of the same order of magnitude as the indentation performed so that the tip also senses the substrate for very small loads and therefore the

Received: July 14, 2015
Revised: October 6, 2015

DOI: 10.1021/acs.langmuir.5b02595
Langmuir XXXX, XXX, XXX−XXX

mechanical properties are dominated by the stiff substrate, resulting in rather large apparent modulus values compared to the bulk one.[17] To avoid the substrate effect (or the so-called double-layer effect), it is widely accepted to limit the indentation depth to less than 10% of the film thickness.[18,19] Interestingly, using a larger indenters radius[20] (and thus reducing the contact strain) does not imply a more accurate measurements of E for hard polymeric thin films[19] (GPa range) and moreover would prevent the resolution of different BCP phases. We experimentally validated those findings, showing that by using standard AFM tips under precise indentation conditions and fitting the data with simple Hertzian models it is possible to reliably measure E with no need for further corrections. Preliminary results previously published[21] give an indication of the proper indentation conditions when the two polymers composing the BCP are polystyrene (PS) and poly(methylmethacrylate) (PMMA), more precisely, poly(styrene-*n*-methilmethacrylate) (PS-*b*-PMMA), generating lamellae-like domains with a 42 nm pitch. PS-*b*-PMMA thin films can self-assemble into ordered periodic structures on the molecular scale (5 to 50 nm) with a rich variety of nanophase-separated structures (lamellar, pillars, etc.). The difference in elastic modulus between the two phases (PS, PMMA) when measured in the bulk is around 0.6 GPa. In this work, we extend the investigation to different PS-*b*-PMMA-based films forming both lamellae and cylinders, analyzing the response of the film at various loads (and thus deformation), describing the mechanical behavior of the polymer phase when indented under precise experimental conditions, and pointing out the force threshold at which the response is no longer purely elastic. We also provide insight into the changes in mechanical properties of the differently oriented domains, for example, measuring the different elastic response of the cylinder structures when vertically or horizontally aligned. We also show that it is possible to overcome typical limitations of friction force microscopy and tapping mode where only the top surface layer is probed. In terms of lateral resolution, we bring the technique to its spatial limits[16] by discriminating nanophase-separated structures with a half pitch of 11 nm. As a final benchmark we measured BCP samples that have undergone several cycles of alumina deposition by atomic layer deposition (ALD), clearly showing how the stiffness increase is limited to the former PMMA domains.

2. MATERIALS AND METHODS

Grafting of the Hydroxyl-Terminated Polystyrene (PS-OH) Brush Layer. The starting substrates are p-type silicon (4−40 Ω·cm resistivity) chips bearing a native silicon oxide layer. In order to achieve segregation and directed self-assembly (DSA) a supporting brush layer is anchored on the bare silicon. The brush layer is created from PS−OH (M_n = 4.5 kg·mol^{-1}, PDI = 1.09), purchased from Polymer Source, Inc. The grafting process starts by coating the silicon surface with the polymer brush. Previously, the silicon surface has been cleaned and activated by O_2 plasma for 10 min to allow the reaction between the hydroxyl groups from the PS−OH and the native oxide of the surface. A 40-nm-thick PS−OH brush layer is deposited by spin coating at 5000 rpm from a 1.5% (w/w) toluene solution. Subsequently, samples are annealed in a nitrogen environment at 260 °C for 5 min. After the samples are annealed, the unreacted PS−OH is rinsed away with toluene by ultrasonication at 40 °C for 5 min, leaving a grafted PS layer of approximately 5 nm.

Block Copolymer Self-Assembly. The BCPs employed were L37 poly(styrene-*n*-methyl methacrylate) (PS-*b*-PMMA 50:50, M_n = 79 kg·mol^{-1}, PDI = 1.13), L22 poly(styrene-*n*-methyl methacrylate) (PS-*b*-PMMA 50:50, M_n = 42.3 kg·mol^{-1}, PDI = 1.1), and C35 poly(styrene-*n*-methyl methacrylate) (PS-*b*-PMMA 69:31, M_n = 60.8 kg·mol^{-1}, PDI = 1.09); the prefix L or C indicates the foreseen segregation configuration (L for lamellae and C for cylinders) while the number indicates the L_0 pitch dimension of the features. The PS-*b*-PMMA powder is dissolved in PGMEA, resulting in a 1.5% (w/w) solution. The block copolymer solution is spin-coated onto the brush layer to obtain a film with a uniform thickness. Afterward, the samples are annealed for 10 min at 230 °C in nitrogen in order to achieve self-assembly, or the so-called "fingerprint" pattern. Film thickness was measured by AFM after gently scratching the film with plastic tweezers (Figure S2 in the Supporting Information).

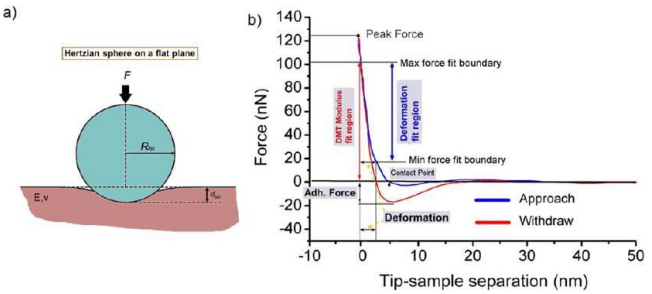

Figure 1. (a) Hertz contact model for a spherical indenter. (b) Typical force plot on a PS reference sample of $E \approx 2.7$ GPa obtained with a cantilever of nominal stiffness K = 42 N/m. All parameters used by the real-time calculation are reported. The deformation is obtained from the approach curve. The minimum force fit boundary and the maximum force fit boundary positions are set at 90 and 15% of the peak force, respectively (approach curve branch), thus the deformation reported is slightly smaller than full deformation. The portion of the withdraw curve used for the fit to obtain the modulus is also indicated.

Atomic Layer Deposition. Alumina was synthesized using binary reactions of trimethylaluminum (TMA, Aldrich, 97%) and water at 85 °C within the polymer films in order to infiltrate the PMMA phase preferentially. The deposition was performed as follows: first, chamber stabilization with nitrogen was performed for 10 min. Then, the precursor, TMA, was admitted into the reactor in predetermined concentrations for 60 s. Afterward, the chamber was purged with nitrogen for 60 s. The same procedure as above was repeated for water. This entire sequence was repeated cyclically. Detailed process parameters are explained elsewhere.[22]

Atomic Force Microscopy. Imaging of surface topography and surface material properties was obtained using an atomic force microscope (AFM) (Dimension Icon, Bruker) operating in peak force tapping mode mounting standard tapping cantilevers (OTESPA and RTESPA, from Bruker; nominal radius of 7 nm) and super sharp tapping cantilevers (TESP-SS, from Bruker, nominal radius of 4 nm) used for both imaging and PeakForce. Cantilever spring constants k range from 26 to 42 N/m, and the tip half angle is less than 18°. The value of the peak force ranged between 5 and 150 nN. This range of cantilever stiffness is particularly suitable for obtaining comparable (therefore detectable) values for the cantilever deflection (d_{cant}) and the sample deformation (d_{sample}) during the nanoindentation experiments, as can be estimated from[12]

$$d_{cant} = \frac{F}{k} \tag{1}$$

$$d_{sample} = \left(\frac{3F}{4E^*\sqrt{R}}\right)^{2/3} \tag{2}$$

where F is the load force, R is the tip radius, and E^* is the sample reduced Young's modulus (d_{sample} here is the indentation calculated with the Hertzian contact model). During measurements in PeakForce the Z-piezo is modulated at a frequency far below the cantilever resonance frequency (2 kHz), and the vertical motion of the cantilever relies on the deflection (force) signal for feedback so that the surface position is acquired when the maximum cantilever deflection (the peak

DOI: 10.1021/acs.langmuir.5b02595
Langmuir XXXX, XXX, XXX−XXX

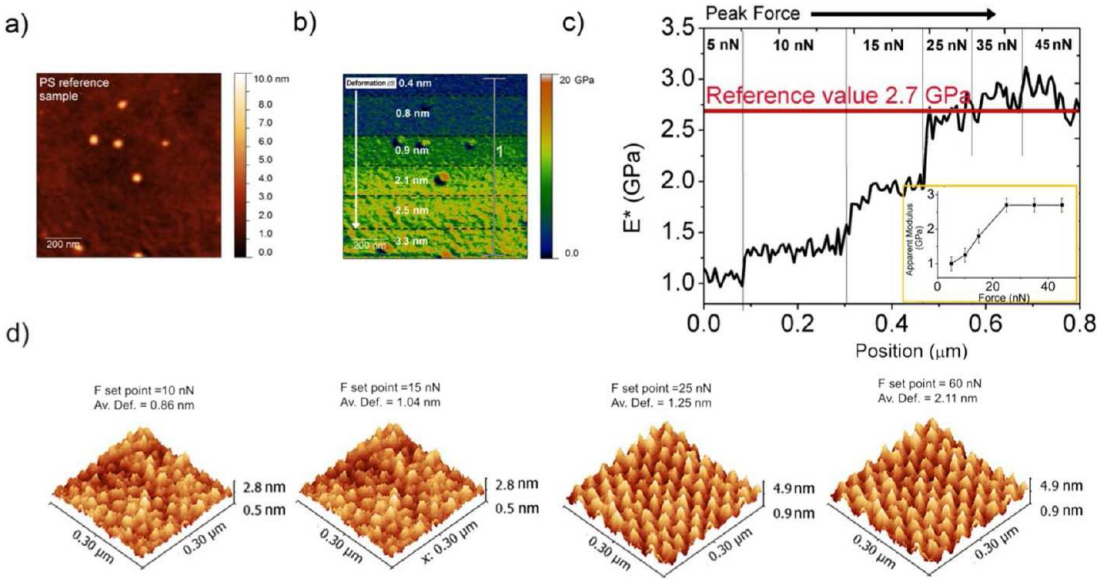

Figure 2. AFM topography: (a) reduced modulus and (b) maps of a PS film used as a reference for calibration. The set point force (peak force) was increased during the scan in order to identify the optimal indentation conditions. The average deformation is reported for each increase in force. In (c) the value of the sample reduced modulus E^* is plotted along profile 1. As the deformation reaches 2.1 nm, the value of E^* does not change with respect to the force applied, matching the reference value ±10%. The inset plots the apparent elastic modulus as a function of peak force. (d) 3D topographies of a C35 sample (vertical cylinders configuration) at various force set points; as deformation approaches 2 nm all circular PMMA domains become clearly visible in the topography.

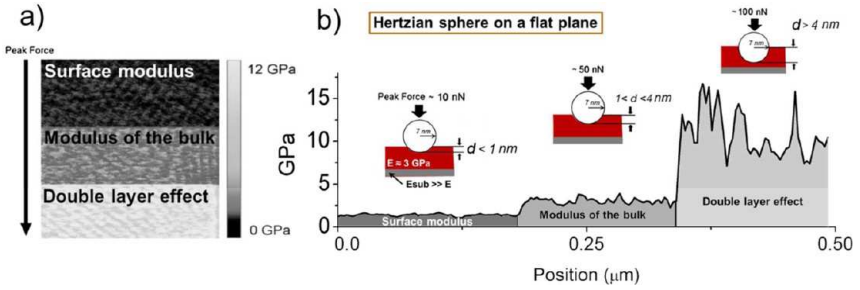

Figure 3. Reduced modulus map (a) of a 40-nm-thick L22 PS-*b*-PMMA BCP film. Three force set points (10, 50, and 100 nN) are applied during the same scan in order to identify the optimal indentation conditions. Spatially averaged reduced Young's modulus values of the whole image along the slow scan direction are plotted in (b). E^* related to the bulk polymer film is measured for deformation d between 1 and 4 nm (center part of panel b). When d exceeds 10% film thickness, the proximity of the stiff substrate begins to influence the measure and the so-called double-layer effect becomes visible.

force) equals the force set-point value. Peak interaction force and material property information is collected for each individual tap. By calibrating of the optical lever sensitivity, cantilever spring constant, and tip radius, the force vs distance curves obtained yield quantitative information such as the elastic modulus, adhesion force, sample deformation and dissipated energy. The deflection sensitivity of the cantilever was calibrated on a hard sapphire substrate. Cantilever axial stiffness was calibrated by the Sader method.[23]

In Figure 1 we report one force vs separation curve obtained with a single approach (blue) and withdraw (red) on a PS reference sample. The various region marked indicates the parameters taken into consideration during the calculation of mechanical properties. The key parameter deformation is defined from a portion of the approach (blue) curve, and it is the parameter represented in the deformation images. The minimum and maximum fit boundary parameters were kept at 90 and 15% of the peak force, respectively, in all experiments. The quantity d (deformation) measured in the experiments is slightly smaller than the full deformation (or d_{sample} at maximum force), being $d \approx 0.75 d_{full}$. The indentation could be eventually measured as the separation from the minimum force to the peak force in the loading curve.

To determine the elastic modulus of the sample the curve is fitted with the Derjaguin–Muller–Toporov (DMT) model,[24] applicable to systems with low adhesion and a small tip radii, using a portion of the unload curve as the fit region. The DMT model is a modified Hertzian model that also takes adhesive forces into account. The reduced modulus E^* comes from the formula

$$F = \frac{4}{3} E^* \sqrt{R d_{sample}^{\ 3}} + F_{adh} \tag{3}$$

Here, F_{adh} is the maximum adhesion force and d_{sample} is the instantaneous sample deformation (that depends on the instantaneous value of the applied force). In the present work we will refer always to the reduced modulus E^*. The relation between E^* and the sample modulus E_s is

$$\frac{1}{E^*} = \frac{1 - \nu_t^{\ 2}}{E_t} + \frac{1 - \nu_s^{\ 2}}{E_s} \tag{4}$$

where ν_t and E_t are the Poisson's ratio and elastic modulus of the tip and ν_s and E_s are the Poisson's ratio and elastic modulus of the sample. Assuming that the tip modulus, E_t, is much larger than the sample modulus ($E_t \approx 160$ GPa), we can neglect the first term. Approximating

DOI: 10.1021/acs.langmuir.5b02595
Langmuir XXXX, XXX, XXX−XXX

ν_s to 0.34 for both PMMA and PS,[6] the relation between the reduced and sample modulus becomes $E_s = 0.88E^*$.

The tip radius values were obtained using a calibration kit from PELCO.[25] By scanning a mica substrate with attached Au spherical nanoparticles of known geometry (nominal particle radius of 5 nm), it is possible to calculate the tip radius (R_{tip}) from the height profile. This method is described in detail elsewhere.[25] Tip radii degrade quickly during the scan, deviating consistently from the nominal value (i.e., 7 nm) in a few scans. Once the tip radius was calculated, we performed a 500 × 500 nm^2 scan at 128 × 128 resolution on the PS reference in order to verify the indentation conditions. A reference sample characterization is shown in the Supporting Information (ESI), Figure S1. The images shown in this article correspond to the first image acquired after tip radius calibration. When the tip radius exceeded 11 nm, the tip was discarded. For simplicity in all figures the nominal radius is taken into account. The topography images were subjected to a second-order polynomial flattening algorithm to correct for surface tilt and bow effects. Some of the modulus images obtained at a 1 × 1 μm^2 scan size were subjected to FFT high-pass filter smoothing in order to remove noise.

3. RESULTS AND DISCUSSION

Identifying Optimal Indentation Conditions. Thin film mechanical properties may vary consistently from bulk values. Apart from the influence of a rigid substrates, other phenomena might influence indentation experiments with AFM.[18,26] The thin film glass-transition temperature may increase or decrease with respect to bulk values depending on the film thickness and the interaction with the supporting substrate.[27] A softer liquidlike layer is probably present at the polymer−air interface,[28] even if its influence could be neglected due to the compression exerted by the tip during indentation. Moreover, end chains with lower surface energy tend to migrate to the surface of glassy polymers.[29] These factors lead to difficulties in the quantitative interpretation of the modulus values obtained and demand for precise indentation conditions for reliable quantitative results.

As a first reference sample we probed a PS film (nominal E value = 2.7 GPa) at various peak force set points (Figure 2). Between 0.4 and 0.9 nm of deformation, the E^* value shows a step (increase) every time the set point peak force is raised (Figure 2b); in addition to that, by representing E^* versus the peak force a minimum threshold for deformation lies between 1 and 2 nm, i.e., a peak force larger than 15 nN is needed, leading to the conclusion that the very top layer is not representative of the intrinsic elastic properties of the material. When deformation is between 2.1 and 3 nm, E^* remains constant as expected, matching the nominal value of the reference sample (2.7 GPa) with 10% variability, within the RMS value of the modulus image (0.26 GPa).

Topography contrast results were also enhanced by optimal indentation condition, as shown in Figure 2d. In this panel, we show 3D topographies of a different sample, the surface of a C35 PS-*b*-PMMA BCP oriented in vertical cylinder morphology. As the topography in peak force is generated at maximum loading, different materials will deform differently, thus contributing to the contrast in the height signal. Height maps taken at lower loads/indentations (15, 25 nN) do represent the topography of the sample surface, but images taken at higher loads (40, 60 nN) capture each polymer domain better, with PMMA domains (vertical cylinders) resulting in higher topography. Real surface topography could eventually be reconstructed, acquired with a very low force set point or from "soft" tapping (i.e., minimizing the tip−sample interaction), resulting in a much flatter surface[30] with a roughness of about 0.3 nm$_{rms}$ (Figure S3 in ESI).

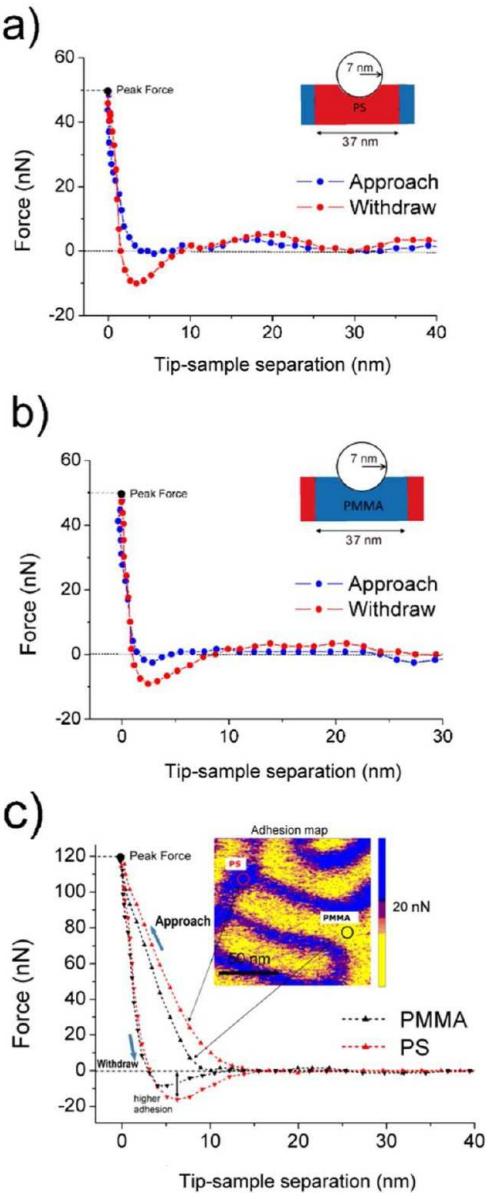

Figure 4. Force curves acquired on an L37 PS-*b*-PMMA BCP thin film. The indentation position lies in the middle of the PS phase (a) and PMMA phase (b), as the two insets illustrate. Approach and withdraw curves overlap in the linear region, showing a purely elastic response. When increased loads are applied (120 nN) the sample undergoes a plastic deformation that is different for each phase (c); the area between the approach and withdraw curves represents the work required to plastically deform the material. The inset in (c) is an adhesion map of the area scanned. Even if topography results are altered by the deformation, in the adhesion channel it is still possible to clearly identify both phases.

After identifying the minimum deformation required for bulk reliable measures, we characterized a 40-nm-thick PS-*b*-PMMA BCP L22 film. As illustrated in Figure 3, the presence of a stiffer substrate becomes visible for peak force loads above 50 nN (d > 4 nm), with such a value matching the empirical estimation. We have thus identified that the optimal deformation must be between 1 and 4 nm for $R \approx 7$ nm.

DOI: 10.1021/acs.langmuir.5b02595
Langmuir XXXX, XXX, XXX−XXX

Table 1. Characteristics of BCP Samples[a]

sample	M_n (kg/mol)	thin film morphology	thickness (nm)	R_0[b]	$E^*_{PS\ phase}$ (GPa)	$E^*_{PMMA\ phase}$ (GPa)
L37	79	vert. lamellae	43	1	1.97 ± 0.21	3.10 ± 0.73
L22	42.3	vert. lamellae	40	1	2.63 ± 0.19	3.08 ± 0.20
C35	60.8	vert. cylinders	42	2.22	2.36 ± 0.25	2.91 ± 0.22
		horiz. cylinders	42		2.09 ± 0.24	2.74 ± 0.27

[a]E^* values correspond to the center of each Gaussian distribution. [b]R_0: molar ratio of PS to PMMA.

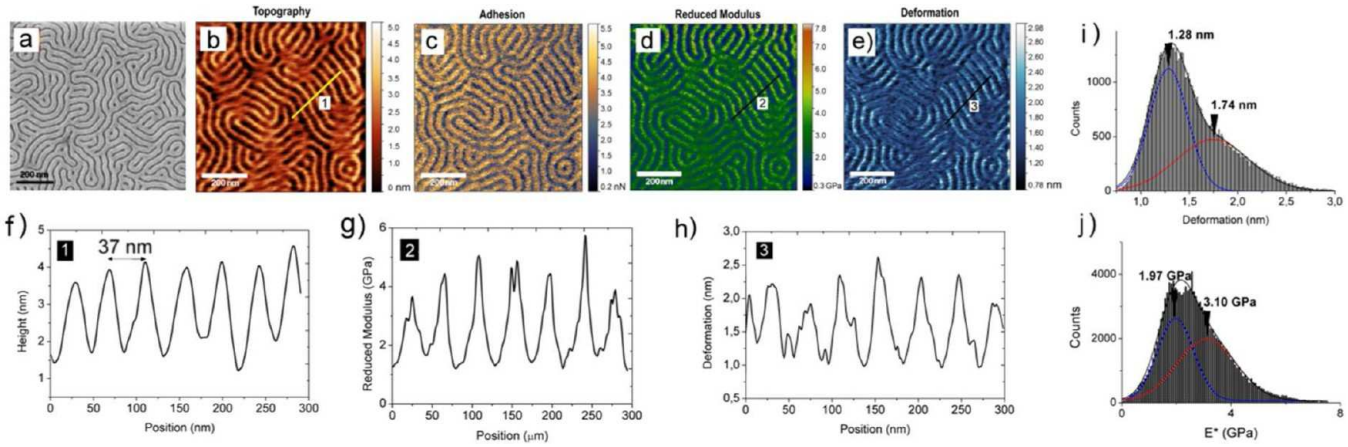

Figure 5. Characterization of a self-assembled L37 PS-*b*-PMMA BCP thin film sample: (a) SEM image of the film after the PMMA phase has been removed by oxygen plasma and then height (b), adhesion (c), elastic (d), and deformation (e) maps of the same sample acquired by peak force tapping at a 30 nN set point. In the graphs below we report the detailed profiles of the topography (f), reduced modulus (g), and deformation (h), with the profiles indicated as 1, 2, and 3, respectively. For deformation and elastic maps the corresponding Gaussian fittings of the data histograms are also reported in (i) and (j).

As it is shown in Figure 4a,b, under the above conditions, approach and withdraw curves overlap in the linear region, showing a purely elastic response. When increased peak force loads are applied (120 nN), the sample undergoes a plastic deformation that is different for each phase (Figure 4c); the area between the approach and withdraw curves represents the work required to plastically deform the material.

Self-Assembled BCP Samples. Three different BCP films have been characterized after the self-assembly, and their characteristics have been summarized in Table 1. In all BCP samples, deformation was kept between 1 and 4 nm. The contrast between the two phases (PS and PMMA) reverses from the modulus (PS phase softer/darker) to deformation and adhesion maps (PS deforms more and always results in higher adhesion as depicted in Figure 4c). The value of E^* reported in Table 1 is obtained by fitting the modulus distribution of a single image (256 × 256 resolution) to two Gaussians, each representing the modulus distribution of each phase. The center of the two distributions is given as a reference reduced modulus. The values of E^* are compatible to the values measured for PS thin films having the same thickness and similar molecular weight at ambient temperature.[31] Deformation distributions have been presented in the same way. Such distributions give additional information regarding the sample probed; in fact, the size of each segregated phase is close to the volume of interaction of the tip. As foreseen, the two peaks (PS and PMMA) are better resolved for wider-pitch BCPs (L37 and C35 vertically oriented cylinders). First we imaged a PS-*b*-PMMA (L37) BCP thin film (43 nm thickness) with a standard silicon tip (OTESPA) under the proper indentation condition (30 nN set point force). Adhesion, modulus, and deformation channels (Figure 5b–d) present enough contrast to distinguish the two segregated phases, with PS and PMMA phases contributing equally to the histogram (Figure 5i). Detailed profiles of Figure 5 show the pitch size (Figure 5f) and the stiffer top of the PMMA phase due to the fact that the probe interacts only with PMMA lamellae (Figure 5g).

In the following measures we imaged a PS-*b*-PMMA (L22) BCP 40-nm-thick film with a standard silicon tip (OTESPA) under the proper indentation condition (30 nN set point force). As is shown in Figure 6, vertical lamellae visible by SEM (Figure 6a) can be also distinguished in all peak force channels (Figure 6b–e) with contrast between PMMA and PS worsening in the modulus image. If we look at the surface stiffness distribution (Figure 6f), the PMMA stiffer component (red Gaussian) is slightly less represented if compared to L37 where the contribution was equal. The two peaks are also less separated, with the PMMA phase almost constant (3.08 GPa) and PS around 2.63 GPa, showing that as the tip radius (in this case, approximately 7 nm) gets closer to the half-pitch size (11 nm) it will be increasingly difficult to distinguish the elastic contribution of each separated phase. If the experimentally determined value of the modulus is influenced by the elastic response of the surrounding volume, then adhesion (Figure 6c) is more related to the properties of the topmost surface and shows a good contrast, which is similar to what happens to the phase signal when similar samples are imaged in tapping mode.

With the next BCP sample, PS-*b*-PMMA C35, the molar ratio of the PS component changes from 1 to 2.22 with the effect of changes in the type of segregation occurring (schematics in Figure 7a). The film thickness chosen produced a so-called mixed morphology[32] in which the PMMA cylindrical nanodomains orient either parallel or perpendicular to the film surface within a few hundred of nanometers (Figure 7b). The

DOI: 10.1021/acs.langmuir.5b02595
Langmuir XXXX, XXX, XXX−XXX

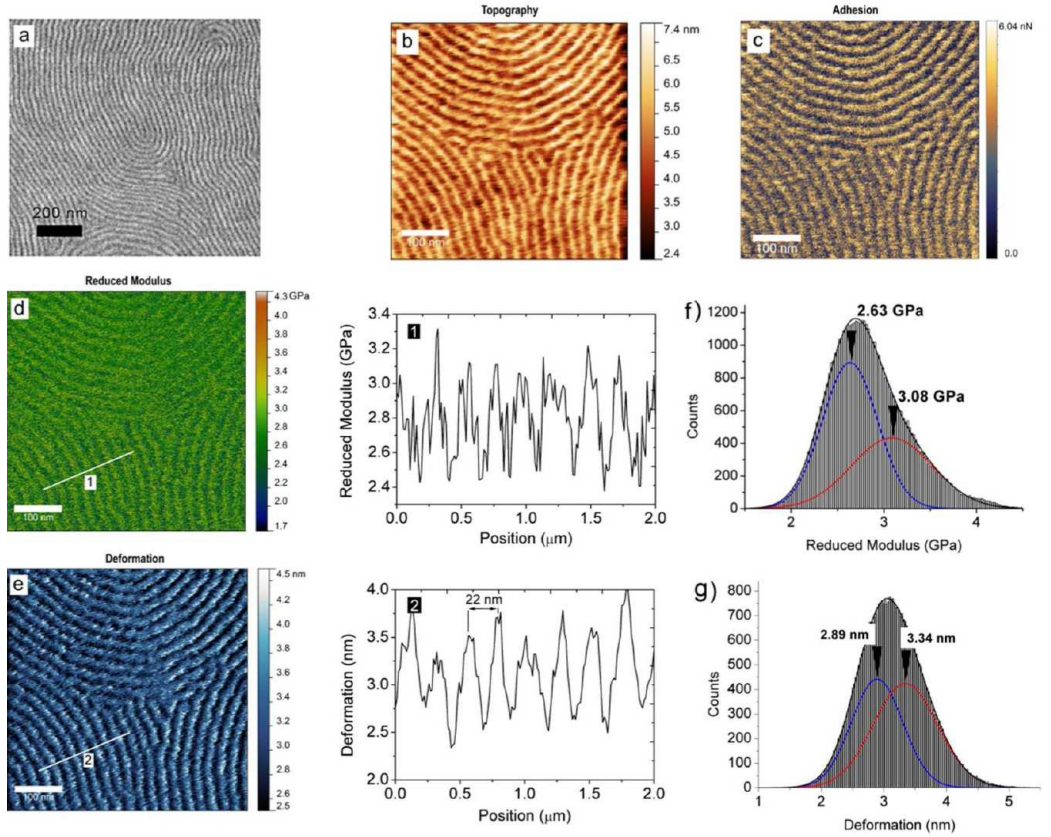

Figure 6. PS-*b*-PMMA L22 BCP sample characterization: (a) SEM image of the film after PMMA removal by oxygen plasma and then (b) height, (c) adhesion, (d) E^*, and (e) deformation maps of a 500 × 500 nm^2 area with vertical lamellae randomly aligned. Reduced modulus and deformation maps are accompanied by a detailed profile, marked as 1 and 2, respectively. For the deformation and elastic map the corresponding Gaussian fittings of the data histograms are also reported in (f) and (g). The adhesion map (c) is shown with an adaptive nonlinear color scale.

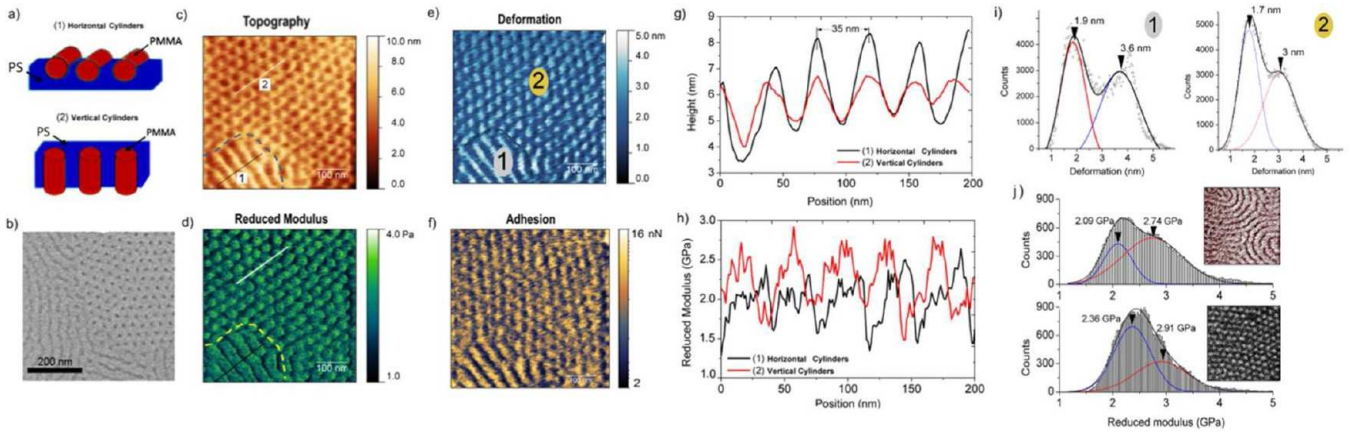

Figure 7. (a) Schematic representation of the two possible phase organization in a C35 PS-*b*-PMMA BCP sample. (b) SEM image of the film after the PMMA phase has been removed with oxygen plasma. In the second column we report the (c) height, (d) elastic, (e) deformation, and (f) adhesion maps of the same sample acquired by peak force tapping. The scanned area presents both configurations: horizontal cylinders (area marked with 1) and vertical (marked with 2). To compare the different areas we report detailed (g) height and (h) modulus profiles. The two histogram in (i) show the difference in deformation between horizontally (1) and vertically (2) aligned cylinders. (j) Modulus histograms of two different scans in which cylinders were aligned horizontally (above) and vertically (below) as depicted in the insets, showing that the PMMA phase is more strongly represented in the horizontal configuration while the vertical configuration shows a stiffening effect of both phases. (d) Reduced modulus and (f) adhesion maps are shown with an adaptive nonlinear color scale.

complete characterization is presented in Figure 7, consisting in a 500 × 500 nm^2 scan acquired with a standard silicon tip (OTESPA) under the proper deformation conditions (20 nN peak force set point). The topography (Figure 7c) presents a left bottom area with cylinders lying horizontally while the rest of the area is filled with cylinders in a vertical position. To predict the elastic behavior of the sample in the two different orientations, we ran a simulation using the structural mechanics module of Comsol Multiphysics 5.0 modeling the indentation of an infinitely rigid sphere (AFM tip apex) into a cylindrical

DOI: 10.1021/acs.langmuir.5b02595
Langmuir XXXX, XXX, XXX−XXX

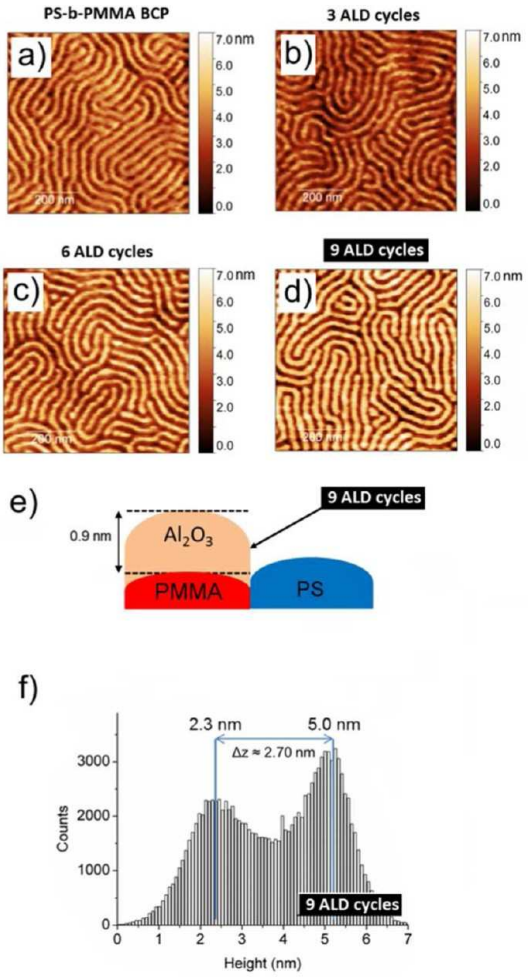

Figure 8. AFM height image acquired in peak force tapping for the PS-*b*-PMMA L37 BCP sample as prepared (a) and topographies after different alumina deposition cycles: three (b), six (c), and nine (d) cycles. The height difference between PMMA (brighter in all images) and the PS phase grows during each ALD step, confirming the preferential deposition of alumina on the PMMA nanodomains. (e) Schematic of the alumina layer final growth. (f) Histogram showing the height distribution of the sample exposed to nine ALD cycles. The height difference between the two phases (Δz) is approximately 2.7 nm and corresponds to the expected growth of nine alumina layers (once Δz_0 is subtracted and the height is corrected by an amount equal to deformation). In order to minimize convolution effects, a supersharp Si tip was used for these experiments.

body (PMMA) with different orientations embedded in a PS matrix on top of a rigid Si layer (details in the SI). As predicted by the simulation and confirmed by the measurements, vertical cylinders appear stiffer if compressed perpendicular to the surface (Figure 7d and detailed profile in Figure 7h). Consequently, deformation obtained in the two areas will be different, as the histograms of Figure 7i show. The two phases are well separated in the deformation distributions with the more rigid PMMA component (narrower red Gaussian curve in Figure 7i) shifting from 1.9 to 1.7 nm average deformation. Two areas with a homogeneous distribution were imaged as well, and the modulus histograms are reported in Figure 7j, showing that the PMMA phase is more strongly represented in the horizontal configuration (larger area under the red Gaussian curve) while in the vertical configuration the PS component (area under the blue Gaussian curve) is largely dominating. Those differences are probably due to different wetting on the top surface, with lamellae and horizontal cylinders presenting a thin wetting top layer largely composed of PS.[33] We also compared the modulus of directed self-assembled areas of the film and randomly aligned areas expecting mild stiffening due to the additional stress built during the directed self-assembly, but we did not notice any appreciable increase or step in the modulus profile after crossing the border between the two areas (Figure S5 in the SI).

ALD-based techniques involve gas-phase molecular assembly reactions to infiltrate polymers with inorganic materials or selectively deposit oxides in order to obtain a certain hardening of the polymeric lithography resists and improve the following pattern-transfer steps. Specifically, the preferential reaction of the trimethylaluminum (TMA) precursor used for Al_2O_3 ALD with PMMA functional groups has been successfully proven for PS-*b*-PMMA diblock copolymer samples.[34,35] For each cycle, selective deposition by ALD produces a selective growth of alumina on top of PMMA domains. In order to verify the localized stiffening and measure the amount of Al_2O_3 deposited, we compared three BCP samples exposed to increasing ADL cycles (3, 6, and 9, respectively) plus a BCP reference sample. As shown in Figure 8 the thickening of the PMMA phase is consistent with the increasing number of cycles run on each sample (Figures 8a–d). In Figure 8f the histogram shows the height distribution of the sample exposed to nine ALD cycles. The height difference between the two phases (Δz) is approximately 2.70 nm and corresponds to the expected growth of nine alumina layers. We can estimate that nine cycles deposit 0.9–1.08 nm of Al_2O_3;[36] once we have subtracted Δz, the initial difference in height between the two phases (Δz_0 = 1.35 nm), plus an additional Δz_d = 0.40 nm corresponding to the local deformation (average obtained from the deformation channel), what remains is a 0.95 nm thickness that lies in the expected range (Figure 8e,f). In Figure 9 the increasing local stiffening of the PMMA phase due to Al_2O_3 deposition is clearly detailed. We report four elastic maps with the same color scale (Figure 9a) for samples exposed to a progressive number of ALD cycles (pristine, three, six, or nine cycles), showing how former PMMA domains become brighter (stiffer). To better detail the deposition we report a line modulus profile of three PMMA phases (Figure 9b); in the graph, it is evident how the PS elastic response remains constant after several ALD cycles while PMMA domains covered by alumina present considerable stiffening (from 3 to 10 GPa). To better describe the effect of ALD we also reported the data histograms of the elastic maps reported in Figure 9a, showing the progressive increase in the stiffer alumina phase on the overall sample area.

4. CONCLUSIONS

Peak force measurements make it possible to access the local mechanical properties of the single segregated phases in BCP ultrathin films, surpassing the limitations of standard nano-indentation methods. Through accurate tip calibration and adjustments of the indentation conditions, avoiding plastic deformation and minimizing the substrate influence, we could discriminate PS and PMMA phases in terms of the surface modulus and adhesion forces, resolving features approaching 10 nm lateral size. Average modulus values of PS and PMMA phases are compatible with existing literature values. Interestingly, the technique is able not only to distinguish compositional differences but also to detect the influence of domain orientation on their elastic response, as found while indenting

DOI: 10.1021/acs.langmuir.5b02595
Langmuir XXXX, XXX, XXX–XXX

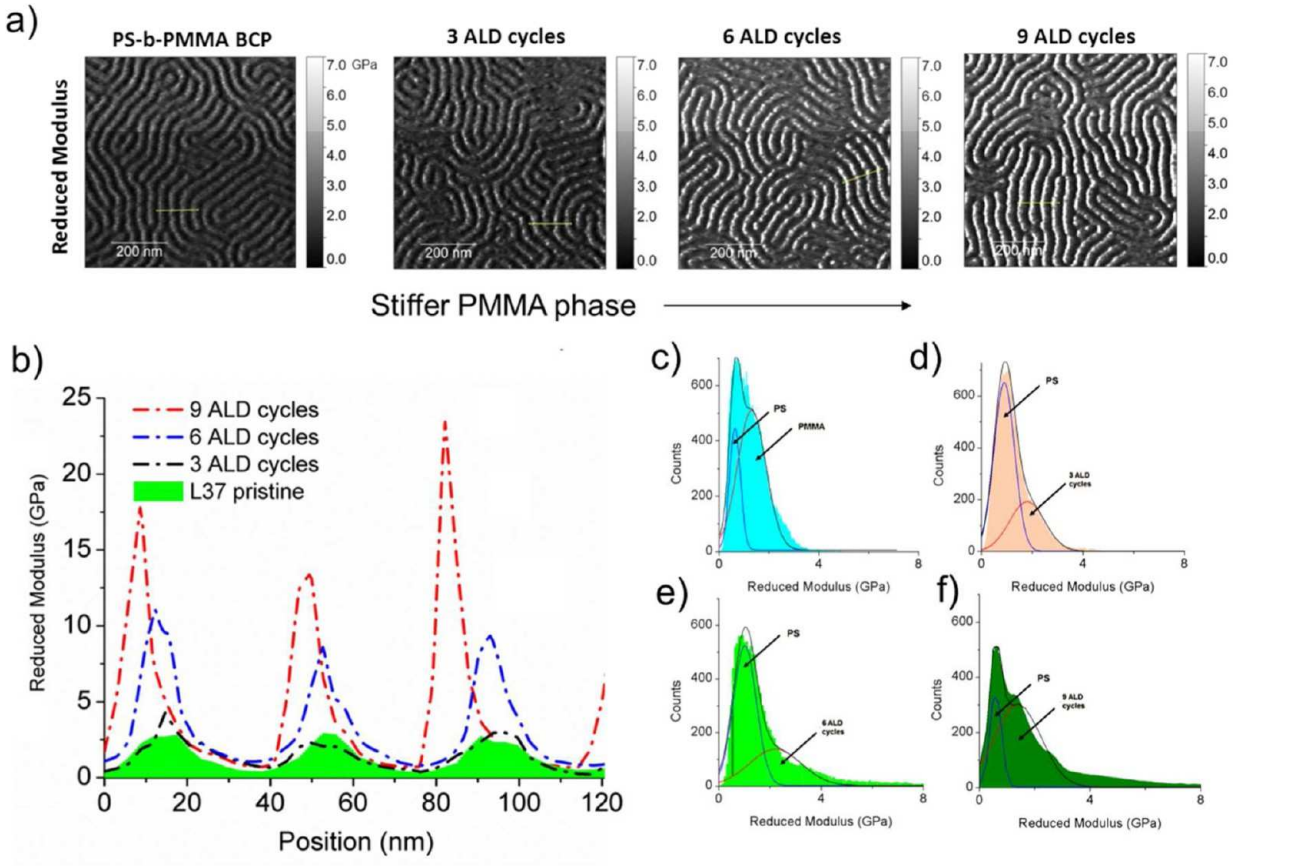

Figure 9. L37 BCP sample stiffening effect due to ALD cycles: (a) AFM elastic map of the BCP "fingerprint" unmodified compared to the elastic map of the same BCP exposed to an increasing number of ALD cycles (three, six, and nine). From left to right, the PMMA phase becomes brighter as expected (the color scale is the same in all four images). (b) Detailed profile of the reduced modulus along three PMMA domains for each sample. It is clear how stiffness increases locally only on former PMMA sites while the PS elastic response remains unchanged. (c–f) Data histograms of the elastic maps reported in (a) showing the progressive increase in the stiffer alumina phase on the overall sample area.

vertical and horizontal PMMA cylinders in a PS matrix. The technique that is shown also has the unique capability of recognizing local stiffening induced by the deposition of alumina, and it is able to recognize the evolution in terms of thickening and stiffening after each ALD cycle, making the peak force an ideal tool for the monitoring of hard mask growth/infiltration in polymers.

■ ASSOCIATED CONTENT

Supporting Information

The Supporting Information is available free of charge on the ACS Publications website at DOI: 10.1021/acs.langmuir.5b02595.

PS reference sample peak force scan, topography, reduced modulus, and deformation maps; AFM topography of a BCP L37 film and related height profile; AFM topography and phase of L37 and C35 BCP films samples; schemes of the model created with Comsol Multiphysics 5.0; AFM peak force images of a bordering area between a randomly oriented and preferentially oriented area of a PS-*b*-PMMA L37 BCP self-assembled sample (PDF)

■ AUTHOR INFORMATION

Corresponding Author

*Tel: +34 93 594 77 00 (ext. 2114). E-mail: matteo.lorenzoni@imb-cnm.csic.es.

Notes

The authors declare no competing financial interest.

■ ACKNOWLEDGMENTS

This paper was written mainly by M.L., and L.E. prepared the BCP samples. All authors have revised and given approval to the final version of the paper. This work was partially funded by projects CoLISA.MMP (ICT project no. 619793), PLACYD (ENIAC 621217 and PCIN-2013-033 MINECO), and FORCE-for-FUTURE (CSD2010-00024).

■ REFERENCES

(1) Stoykovich, M. P.; Nealey, P. F. Block Copolymers and Conventional Lithography. *Mater. Today* **2006**, *9* (9), 20–29.

(2) Hawker, C. J.; Russell, T. P. Block Copolymer Lithography: Merging "Bottom-Up" with "Top-Down" Processes. *MRS Bull.* **2005**, *30*, 952–966.

(3) Bates, F. Block Copolymer Thermodynamics: Theory And Experiment. *Annu. Rev. Phys. Chem.* **1990**, *41* (1), 525–557.

(4) Hu, H.; Gopinadhan, M.; Osuji, C. O. Directed Self-Assembly of Block Copolymers: A Tutorial Review of Strategies for Enabling Nanotechnology with Soft Matter. *Soft Matter* **2014**, *10*, 3867–3889.

DOI: 10.1021/acs.langmuir.5b02595
Langmuir XXXX, XXX, XXX–XXX

(5) Fernández-Regúlez, M.; Evangelio, L.; Lorenzoni, M.; Fraxedas, J.; Pérez-Murano, F. Sub-10 Nm Resistless Nanolithography for Directed Self-Assembly of Block Copolymers. *ACS Appl. Mater. Interfaces* **2014**, *6* (23), 21596−21602.
(6) Briscoe, B. J.; Fiori, L.; Pelillo, E. Nano-Indentation of Polymeric Surfaces. *J. Phys. D: Appl. Phys.* **1998**, *31*, 2395−2405.
(7) Cohen, S. R.; Kalfon-Cohen, E. Dynamic Nanoindentation by Instrumented Nanoindentation and Force Microscopy: A Comparative Review. *Beilstein J. Nanotechnol.* **2013**, *4*, 815−833.
(8) Krämer, G.; Griepentrog, M.; Bonaccurso, E.; Cappella, B. Study of Morphology and Mechanical Properties of Polystyrene−polybutadiene Blends with Nanometre Resolution Using AFM and Force−distance Curves. *Eur. Polym. J.* **2014**, *55*, 123−134.
(9) Voss, A.; Stark, R. W.; Dietz, C. Surface versus Volume Properties on the Nanoscale: Elastomeric Polypropylene. *Macromolecules* **2014**, *47*, 5236−5245.
(10) Sababi, M.; Kettle, J.; Rautkoski, H.; Claesson, P. M.; Thormann, E. Structural and Nanomechanical Properties of Paperboard Coatings Studied by Peak Force Tapping Atomic Force Microscopy. *ACS Appl. Mater. Interfaces* **2012**, *4* (10), 5534−5541.
(11) Rico, F.; Su, C.; Scheuring, S. Mechanical Mapping of Single Proteins at Subnanometer Resolution Using AFM. *Biophys. J.* **2011**, *100*, 23a.
(12) Young, T. J.; Monclus, M. a; Burnett, T. L.; Broughton, W. R.; Ogin, S. L.; Smith, P. a. The Use of the PeakForce TM Quantitative Nanomechanical Mapping AFM-Based Method for High-Resolution Young's Modulus Measurement of Polymers. *Meas. Sci. Technol.* **2011**, *22* (12), 125703.
(13) Martinez-Martin, D.; Herruzo, E. T.; Dietz, C.; Gomez-Herrero, J.; Garcia, R. Noninvasive Protein Structural Flexibility Mapping by Bimodal Dynamic Force Microscopy. *Phys. Rev. Lett.* **2011**, *106* (19), 1−4.
(14) Sahin, O.; Magonov, S.; Su, C.; Quate, C. F.; Solgaard, O. An Atomic Force Microscope Tip Designed to Measure Time-Varying Nanomechanical Forces. *Nat. Nanotechnol.* **2007**, *2* (8), 507−514.
(15) García, R.; Magerle, R.; Perez, R. Nanoscale Compositional Mapping with Gentle Forces. *Nat. Mater.* **2007**, *6* (6), 405−411.
(16) Herruzo, E. T.; Perrino, A. P.; Garcia, R. Fast Nanomechanical Spectroscopy of Soft Matter. *Nat. Commun.* **2014**, *5*, 3126.
(17) Cappella, B.; Silbernagl, D. Nanomechanical Properties of Polymer Thin Films Measured by Force−distance Curves. *Thin Solid Films* **2008**, *516* (8), 1952−1960.
(18) Du, B.; Tsui, O.; Zhang, Q.; He, T. Study of Elastic Modulus and Yield Strength of Polymer Thin Films Using Atomic Force Microscopy. *Langmuir* **2001**, *17* (11), 3286−3291.
(19) Oommen, B.; Van Vliet, K. J. Effects of Nanoscale Thickness and Elastic Nonlinearity on Measured Mechanical Properties of Polymeric Films. *Thin Solid Films* **2006**, *513*, 235−242.
(20) Dimitriadis, E. K.; Horkay, F.; Maresca, J.; Kachar, B.; Chadwick, R. S. Determination of Elastic Moduli of Thin Layers of Soft Material Using the Atomic Force Microscope. *Biophys. J.* **2002**, *82* (5), 2798−2810.
(21) Lorenzoni, M.; Evangelio, L.; Nicolet, C.; Navarro, C.; San Paulo, A.; Perez Murano, F. Nanomechanical Properties of Solvent Cast PS and PMMA Polymer Blends and Block Co-Polymers. *Proc. SPIE* **2015**, 942325.
(22) Oria, L.; Ruiz De Luzuriaga, a.; Alduncin, J. a.; Perez-Murano, F. Polystyrene as a Brush Layer for Directed Self-Assembly of Block Co-Polymers. *Microelectron. Eng.* **2013**, *110*, 234−240.
(23) Sader, J. E.; Chon, J. W. M.; Mulvaney, P. Calibration of Rectangular Atomic Force Microscope Cantilevers. *Rev. Sci. Instrum.* **1999**, *70* (10), 3967.
(24) Cappella, B.; Dietler, G. Force-Distance Curves by Atomic Force Microscopy. *Surf. Sci. Rep.* **1999**, *34* (1−3), 1−104.
(25) Vesenka, J.; Manne, S.; Giberson, R.; Marsh, T.; Henderson, E. Colloidal Gold Particles as an Incompressible Atomic Force Microscope Imaging Standard for Assessing the Compressibility of Biomolecules. *Biophys. J.* **1993**, *65* (3), 992−997.
(26) Stafford, C. M.; Harrison, C.; Beers, K. L.; Karim, A.; Amis, E. J.; VanLandingham, M. R.; Kim, H.-C.; Volksen, W.; Miller, R. D.; Simonyi, E. E. A Buckling-Based Metrology for Measuring the Elastic Moduli of Polymeric Thin Films. *Nat. Mater.* **2004**, *3*, 545−550.
(27) Wallace, W. E.; Van Zanten, J. H.; Wu, W. L. Influence of an Impenetrable Interface on a Polymer Glass-Transition Temperature. *Phys. Rev. E: Stat. Phys., Plasmas, Fluids, Relat. Interdiscip. Top.* **1995**, *52* (4).R332910.1103/PhysRevE.52.R3329
(28) Keddie, J. L.; Jones, R. a L.; Corey, R. a. Size-Dependent Depression of the Glass Transition Temperature in Polymer Films. *Europhys. Lett.* **1994**, *27*, 59−64.
(29) Tanaka, K.; Jiang; Nakamura, K.; Takahara, A.; Kajiyama, T.; Ishizone, T.; Hirao, A.; Nakahama, S. Effect of Chain End Chemistry on Surface Molecular Motion of Polystyrene Films. *Macromolecules* **1998**, *31* (15), 5148−5149.
(30) Knoll, R.; Magerle, K.; Krausch, G. Tapping Mode Atomic Force Microscopy on Polymers: Where Is the True Sample Surface? *Macromolecules* **2001**, *34* (12), 4159−4165.
(31) Torres, J. M.; Stafford, C. M.; Vogt, B. D. Impact of Molecular Mass on the Elastic Modulus of Thin Polystyrene Films. *Polymer* **2010**, *51* (18), 4211−4217.
(32) Zucchi, I. a; Poliani, E.; Perego, M. Microdomain Orientation Dependence on Thickness in Thin Films of Cylinder-Forming PS-B-PMMA. *Nanotechnology* **2010**, *21* (18), 185304.
(33) Borah, D.; Ghoshal, T.; Shaw, M. T.; Chaudhari, A.; Petkov, N.; Bell, A. P.; Holmes, J. D.; Morris, M. a. The Morphology of Ordered Block Copolymer Patterns as Probed by High Resolution Imaging. *Nanomater. Nanotechnol.* **2014**, 1.
(34) Biswas, M.; Libera, J. A.; Darling, S. B. New Insight into the Mechanism of Sequential In Filtration Synthesis from Infrared Spectroscopy. *Chem. Mater.* **2014**, *26*, 6135.
(35) Tseng, Y. C.; Peng, Q.; Ocola, L. E.; Elam, J. W.; Darling, S. B. Enhanced Block Copolymer Lithography Using Sequential Infiltration Synthesis. *J. Phys. Chem. C* **2011**, *115* (36), 17725−17729.
(36) Wilson, C. a; Grubbs, R. K.; George, S. M. Nucleation and Growth during Al 2 O 3 Atomic Layer Deposition on Polymers. *Chem. Mater.* **2005**, *17* (23), 5625−5634.

DOI: 10.1021/acs.langmuir.5b02595
Langmuir XXXX, XXX, XXX−XXX